



Nanostructured Pd–Pt nanoparticles: evidences of structure/performance relations in catalytic H₂ production reactions

Matteo Monai^{a,b,*}, Tiziano Montini^{a,b}, Emiliano Fonda^c, Matteo Crosera^a, Juan José Delgado^d, Gianpiero Adami^a, Paolo Fornasiero^{a,b,*}

^a Department of Chemical and Pharmaceutical Sciences, University of Trieste, via L. Giorgieri 1, 34127 Trieste, Italy

^b ICCOM-CNR URT Trieste, Consortium INSTM Trieste Research Unit, via L. Giorgieri 1, 34127 Trieste, Italy

^c Synchrotron SOLEIL, L'Orme des Merisiers, Saint Aubin, BP48 91192 Gif sur Yvette Cedex, France

^d Departamento de Ciencia de los Materiales e Ingeniería Metalúrgica y Química Inorgánica, Facultad de Ciencias, Universidad de Cádiz, 11510 Puerto Real, Spain



ARTICLE INFO

Keywords:

Palladium
Bimetallic catalyst
Structure-activity relationship
Nanoparticles
Hydrogen production

ABSTRACT

A widespread approach to modulate the performances of heterogeneous catalysts is the use of bimetallic nanoparticles (NPs) as the active phase. However, studying the relationship between the NPs structure and catalytic properties requires well-defined systems, having uniform composition, size and nanostructure, which cannot be achieved by traditional methods (e.g. impregnation). Here, we developed wet-chemistry synthetic routes to prepare Pd–Pt NPs or Pt-core@Pd-shell NPs of small size and well-controlled composition and structure, protected by mercaptoundecanoic acid (MUA) moieties. The pristine NPs were tested for H₂ production by NH₃BH₃ hydrolysis, in order to systematically investigate the effect of composition and of synthetic route on the activity of the systems. Depending on the preparation method, two distinct trends of activity were observed, rationalized in terms of the extent of surface functionalization by MUA. The MUA protective layer was found to effectively stabilize the NPs dispersion while maintaining high activity in certain cases (Pt-rich NPs), and was demonstrated to be essential for catalyst recycling. In order to further study structure-activity relationships of Pd–Pt NPs after ligand removal, nanostructured Pd–Pt@CeO₂-based catalysts were prepared by self-assembly route. Regardless of the starting NPs structure (alloy or core-shell), similar water gas shift reaction performances were observed, due to the structural rearrangements occurring upon oxidation and reduction thermal treatments, which led to the formation of Pt-rich core@Pd–Pt-shell under reducing conditions.

1. Introduction

The synthesis of metal and metal oxide nanoparticles (NPs) of controlled composition, dimension and morphology has led to a better understanding of the way catalysts work and how to improve their activity [1,2]. Bimetallic NPs have attracted increasing attention in view of their particular activity, selectivity or stability, arising from the interplay between the two components [3–5]. Notably, the performances of bimetallic catalysts not only depend on the active phase composition, but also on the chemical state of each component [5] and on the particles nanostructure (e.g. alloy, core-shell systems) [6]. Advanced structure/activity studies in environmental and energy-related applications of bimetallic NPs-based systems can give new insights in how to develop more performing catalysts, as recently demonstrated for biofuels upgrading [5] and methane catalytic oxidation [3].

Pd–Pt bimetallic catalysts have been studied in many catalytic reactions, such as hydrogenation of aromatics [7,8], hydrodesulfurization

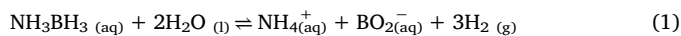
reaction [9], electro-oxidation of methanol [10], oxygen reduction[11] and catalytic combustion [12,13] sometimes showing improved activity and/or stability with respect to their monometallic counterparts. For instance, in methane catalytic combustion, Pd–Pt -based catalysts prepared by conventional methods showed increased tolerance towards two main deactivating agents typically found in real application, i.e. sulfur compounds [14] and water vapor [15]. More recently, uniform Pd–Pt nanocrystals were shown to be more stable towards water vapor aging under methane combustion conditions [3].

To investigate the reason of improved performances of bimetallic catalysts, it is fundamental to obtain metal NPs with controlled and uniform composition and morphology. Wet chemical methods such as solvothermal and colloidal synthesis can be used to obtain such precise systems [16]. Here, we modified a previously reported synthesis of functionalized Pd nanoparticles [17], developing two different strategies aimed to obtain alloyed Pd–Pt NPs or Pt-core@Pd-shell NPs. Alloy formation was pursued by co-reducing Pd and Pt precursors with

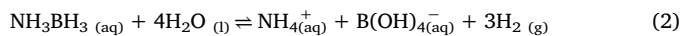
* Corresponding authors at: Department of Chemical and Pharmaceutical Sciences, University of Trieste, via L. Giorgieri 1, 34127 Trieste, Italy.
E-mail addresses: matteo.monai@phd.units.it (M. Monai), pforasiero@units.it (P. Fornasiero).

NaBH_4 (co-reduced, CoRed), while Pt@Pd systems were synthesized by introducing pre-formed Pt NPs in the solution of Pd precursor right before reduction (pre-reduced, PreRed). Mercaptoundecanoic acid (MUA) was chosen as the stabilizing organic ligand since it has both a mercapto-group, which binds to the NPs surface preventing agglomeration, and a carboxylic terminal group, which can be exploited to synthesize nanostructured composite for catalytic applications [18,19]. Moreover, thiols were recently demonstrated to play a critical role in the synthesis of small alloyed NPs (~ 2 nm diameter), by formation of multinuclear metal–thiolate complexes, which favor intimate mixing of the metals [20].

Structure–activity studies were carried out on Pd–Pt-MUA NPs dispersions for NH_3BH_3 (ammonia borane, AB) catalytic hydrolysis. AB is an interesting material for solid hydrogen storage and controlled generation in fuel cell systems, owing to its high hydrogen gravimetric content (19.6 wt.%), possible efficient regeneration [21], non-toxicity and stability in neutral and basic aqueous solutions [22,23]. Hydrogen generation from AB can be achieved by thermolysis, hydrolysis and dehydrogenation, but in all cases harsh conditions are required unless a proper catalyst is used [24]. The hydrolysis reaction has often been described according to the reaction:



While recent kinetic studies [25,26] evidenced that the reaction proceeds via:



In any case, 3 mol H_2 can be produced by hydrolysis of 1 mol AB [27]. Transition metal NPs have been widely investigated for this reaction [28–32], and bimetallic systems were reported to have enhanced catalytic properties [28–30], but limited work was dedicated to the effect of the NPs composition or structure under the exclusion of particle size effects [25]. This is a crucial point since the hydrolytic dehydrogenation of AB is a well-known structure-sensitive reaction. Here, careful characterization of a wide array of $\text{Pd}_x\text{Pt}_{1-x}$ -MUA NPs allowed to evidence compositional- and structural-dependent activity trends, providing valuable insights for the development of efficient colloidal catalysts. Alkaline conditions were selected to stabilize AB against unwanted spontaneous hydrolysis and to effectively disperse the Pd–Pt-MUA NPs.

The MUA functionalization of the NPs was exploited for the production of catalysts based on Pd–Pt@CeO₂ units, prepared by self-assembly of the NPs with Ce decyloxide, followed by controlled hydrolysis and deposition on a high surface area Si-Al₂O₃ support [18,19]. Similar Pd@CeO₂-based catalysts have shown remarkable activity for CO oxidation and methane catalytic combustion, but they deactivated under gas shift reaction (WGSR, $\text{CO} + \text{H}_2\text{O} \leftrightarrow \text{CO}_2 + \text{H}_2$) conditions, due to lower accessibility of Pd to the gas phase due to encapsulation by partially reduced CeO₂ [33,34]. Nonetheless, CeO₂-supported catalysts are known to be orders of magnitude more active in the WGSR than metals on other supports, mainly in reason of the redox properties of CeO₂, able to act as an oxygen buffer oxidizing the CO adsorbed on metal nanoparticles and being oxidized back by H₂O vapor [35–39].

Here, we investigated the effect of the active phase composition in Pd–Pt@CeO₂-based catalysts, with the aim of obtaining active and stable nanostructured catalysts for the WGSR. Moreover, the structural evolution of the Pd–Pt active phase after oxidizing and reducing thermal treatments was elucidated by *in situ* X-ray absorption experiments and correlated with the observed WGSR catalytic performances.

2. Experimental

2.1. Catalyst synthesis

Potassium tetrachloropalladate (II) (32.04 wt.% as Pd) and

potassium tetrachloroplatinate (II) (46.71 wt.% as Pt) were purchased from ChemPUR. Sodium borohydride (98%+) was purchased from Acros Organics. Sodium hexachloroplatinate (IV) (98%), cerium ammonium nitrate (CAN, 99.99%), sodium methoxide (25% in methanol), phosphoric acid (85%), 11-mercaptoundecanoic acid (MUA, 95%), 1-dodecanethiol (DT, ≥98%) dodecanoic acid (99%), triethoxy(octyl)silane (TEOOS, 97.5%), and all the solvents (analytical grade) were purchased from Sigma–Aldrich.

The Pd–Pt nanoparticles were synthesized following two different procedures, referred to as co-reduction and pre-reduction. The two routes are based on a previously reported synthesis of Pd-mercaptopoundecanoic acid (MUA) nanoparticles [17] and only differ in the Pt introduction method. In the co-reduction route, K₂PtCl₆ was added together with K₂PdCl₆ (0.2 mmol total, Pd:Pt molar ratio adjusted to the desired product) at the beginning of the synthesis. Briefly, the precursors were dissolved in a mixture of 5 mL water and 25 mL acetone. MUA (0.5:1 mol vs total metal) and concentrated H₃PO₄ (60:1 mol vs total metal) were added, and finally a NaBH₄ aqueous solution (0.5 M, 10 mol vs total metal) was used as a reducing agent to obtain the NPs. The system was then evaporated and the NPs were washed with water (2 × 10 mL) and EtOH (2 × 10 mL) to eliminate all the reaction by-products. Finally, they were dissolved in THF (0.5 mg/mL total metal). In the pre-reduction route, a dispersion of pre-formed Pt NPs in EG (3 mg/mL as Pt) was added to the solution containing K₂PdCl₆ and MUA before addition of NaBH₄. Pure Pd-MUA NPs were produced in this way, without adding any Pd salt to the synthetic mixture. The starting Pt NPs were prepared according to a literature procedure and added as synthesized [40].

Pd–Pt@CeO₂ units were prepared according to the procedure reported in the literature for Pd@CeO₂ units [41]. Briefly, PdPt-MUA nanoparticles dispersed in THF were added to a THF solution of cerium (IV) tetrakis(decyloxide) (Ce(OR)₄), followed by the addition of a THF solution of dodecanoic acid. Ce(OR)₄ was prepared dissolving 5.00 g of CAN in 50 mL methanol (MeOH), followed by addition of 1-decanol (6.97 mL, 4 mol vs Ce). Then, a 25 wt% solution of MeONa in MeOH (12.51 mL, 6 mol vs Ce) was added dropwise to the solution, causing formation of gaseous NH₃ and precipitation of cerium(IV) methoxide and NaNO₃. After 1 h of stirring, the solvent was removed by evaporation to yield an oil (orange color) mixed with solid NaNO₃. The oil was dissolved in 25 mL dichloromethane (DCM), and the solvent was evaporated again. This procedure was repeated twice, after which 25 mL DCM were added, the solid was filtered out, and DCM was removed by evaporation. The orange-oil product was used without further purification. For the synthesis of Pd@CeO₂ units, 10 mL of the THF solution of Pd–Pt-MUA nanoparticles (0.5 mg/mL as total metal) were slowly added to 5 mL THF solution of Ce alkoxide to obtain a final metal:CeO₂ weight ratio of 1:9, followed by the addition of dodecanoic acid (1 mol vs Ce) dissolved in 10 mL of THF. Hydrolysis of the metal alkoxide in the Pd–Pt–Ce solution was carried out by slowly adding 1.2 mL of H₂O dissolved in 10 mL of THF over a period of 4 h (120 mol vs Ce). For preparation of the final catalysts used in the WGSR, the Pd–Pt@CeO₂ units were adsorbed in monolayer form onto modified, hydrophobic γ-Al₂O₃, prepared by reaction of 1.0 g calcined γ-Al₂O₃ with 0.55 mL TEOOS, in 20 mL toluene at reflux for 3 h. The powder was used for synthesis after washing with toluene (2 × 20 mL, centrifugation at 4500 rpm, 5 min) and drying at 120 °C overnight [18]. The Pd–Pt(1%)@CeO₂/Si-Al₂O₃ catalysts were then either oxidized *in situ* at 250 °C before the reaction or calcined at 500 °C in air for 5 h, in order to remove the organic components and to activate the catalyst [18]. For comparison, Pd(1%)@CeO₂/Si-Al₂O₃ and Pt(1%)@CeO₂/Si-Al₂O₃ catalyst were prepared starting from Pd-MUA and Pt-MUA NPs, respectively.

2.2. Characterization techniques

For Inductively Coupled Plasma–Optical Emission Spectroscopy

(ICP-OES) analysis, 2 mL of Pd–Pt-MUA solution 0.5 mg/mL in THF were picked up and put in a 25 mL round bottom flask. THF was evaporated at rotary evaporator. 2 mL aqua regia ($\text{HNO}_3\text{:HCl}$ mixture, 1:3 in volume) were added to dissolve the Pd–Pt NPs. The solution was diluted with DI water to 50 mL. Total Pt and Pd concentrations in the samples were quantified using an Optima 8000 instrument (Perkin Elmer; Waltham, MA, USA) with an integrated autosampler (S10, Perkin Elmer; Waltham, MA, USA). A five-point standard calibration curve was used for ICP-OES measurements (range 0–100 mg L⁻¹). The limits of detection at the operative wavelengths (Pd 340.458 nm, Pt 265.945 nm, S 181.975 nm) were 0.05 mg L⁻¹ for Pd and Pt and 0.10 mg L⁻¹ for S. The precision of the measurements as repeatability (as RSD%) for the analysis was always less than 5%.

Pd and Pt accessibility in Pd–Pt@CeO₂/Si-Al₂O₃ catalysts was estimated by low temperature CO chemisorption measurements. Typically, 150 mg of 500 °C calcined sample were pre-reduced at 80 °C in 5.0% H₂/Ar for 30 min, degassed for 30 min at 80 °C and for 4 h at 350 °C. The samples were then cooled to –80 °C using an acetone-dry ice bath and exposed to between 2 and 20 Torr of CO. Equilibrium was considered to have been reached when the pressure change was less than 0.01% for 11 consecutive readings, taken at 30-s intervals. Adsorbed volumes were determined by extrapolation of the linear part of the adsorption isotherm to zero pressure. A 1:1 chemisorption stoichiometry ratio was assumed for CO/Pd and CO/Pt.

The microstructure of the samples was analyzed by Transmission Electron Microscopy (TEM). The characterization was performed on a JEOL 2010FEG microscope operated in Scanning mode (STEM) using a spot of 0.5 nm and the images were recorded with a High-Angle Annular-Dark-Field (HAADF) detector and a camera length of 10 cm. The microscope is equipped with an Oxford SDD Detector (X-Max 80 system) that allow to gain chemical information of single nanoparticles by obtaining point Energy-dispersive X-ray spectrum (EDS).

For pristine Pd–Pt-MUA NPs characterization by Extended X-Ray Absorption Fine Structure (EXAFS), the NPs dispersions in THF were deposited on BN right after the synthesis so to achieve an acceptable $\Delta\mu_x$, dried, pressed in tablets and sealed in Kapton tape. Samples were measured at room temperature at the SAMBA beamline [42] in transmission mode. Data of high quality were obtained even for $\Delta\mu_x$ below 0.1 and this enabled us to obtain numerical results on a large number of samples.

For *in situ* XAS Pd–Pt@CeO₂/Si-Al₂O₃ powders were diluted with BN and loaded in the cell described in details elsewhere [43]. The samples were calcined *in situ* to 250 °C for 30 min in O₂(5%)/He. After the treatment, the sample was cooled to room temperature and EXAFS spectra were collected at Pd K edge and Pt L₃ edge. Then, the sample were reduced to 250 °C for 30 min in H₂(5%)/Ar. After cooling to room temperature, EXAFS were collected again. EXAFS data analysis have been carried on with theoretical standards from Feff 8.4 [44] and with the software Horae [45] for data handling and fitting. All fits have been carried out in r-space.

2.3. Catalytic measurements

The Pd–Pt-MUA NPs were tested for NH₃BH₃ hydrolysis in basic aqueous solutions. In order to perform the catalytic tests, the NPs dispersion in THF was evaporated and the NPs were re-dispersed in a 100 mM NaOH solution (0.1 mM Pd–Pt total concentration). 20 mL of the resulting Pd–Pt-MUA solution were introduced in a sealed reactor, connected to a GC analyzer, and the solution was purged with Ar. After 5 min, a 5 mL aqueous solution of 61.7 mg NH₃BH₃ (2 mmol) was injected with a syringe under Ar flow. The final metal/NH₃BH₃ molar ratio was 1/1000. In recycling experiments, the NPs dispersion was transferred to a centrifuge tube, and some droplets of HNO₃ (conc.) were added to the NPs solution until precipitation occurred. The NPs were washed 3 times with water (10 mL) and finally redispersed in a 100 mM NaOH solution by sonication. Such basic solution was then

used in the successive catalytic run. The H₂ concentration in the effluent stream from the reactor was monitored on-line using an Agilent 7890 gas chromatograph equipped with a TCD detector connected to a MolSieve 5A column. Blank experiments without Pd–Pt-MUA NPs did not show any H₂ evolution.

The Pd–Pt@CeO₂/Si-Al₂O₃ catalysts were tested in the WGSR. Typically, 40 mg of catalyst was loaded in a tubular reactor, pretreated under O₂(5%)/Ar or H₂(5%)/Ar and it was finally exposed to reaction conditions. The reaction was carried out at atmospheric pressure, in 7.6 Torr CO and 38 Torr H₂O, Ar balance, at a gas hourly space velocity (GHSV) of 75,000 h⁻¹ (total flow rate of 48.5 mL/min). Water was introduced to the reactor by means of a Gas-Tight syringe, controlled by an infusion pump, while the partial pressures of CO and Ar were adjusted using mass flow controllers. The composition of the effluent gas was typically analyzed online using a mass spectrometer. In selected experiments, the reactor exhaust was monitored using an Agilent 7890 gas chromatograph equipped with two analytical lines. A TCD detector, connected to a MolSieve 5A column using Ar as carrier, was used to monitor H₂ concentration while a FID detector, connected to a Select Permanent Gases/CO₂ column using He as carrier and a methanator, was used to monitor CO, CH₄ and CO₂.

3. Results and discussion

3.1. Pd–Pt-MUA NPs synthesis and characterization

The Pd-MUA, Pt-MUA and Pd–Pt-MUA NPs prepared by CoRed and PreRed routes (see Experimental Method) were characterized by ICP-OES, TEM-EDS and EXAFS at the Pd K and Pt L₃ edges. Pd-MUA NPs of 1.5–2.0 nm were obtained in accordance with previously reported result (Fig. 1) [46]. Pt-MUA NPs of similar size were obtained by functionalizing pre-formed Pt NPs with MUA (supported by EXAFS results, *vide infra*), following the PreRed synthetic procedure in the absence of Pd precursor (Fig. 1).

As revealed by ICP-OES analysis, the PreRed method allowed to synthesize Pd–Pt-MUA NPs in the entire compositional range, with the expected Pd:Pt molar ratio. The yield of the synthesis calculated basing on ICP-OES results was higher than 95% for both metals, in all cases. On the other hand, the CoRed procedure could only yield Pd-rich NPs, due to a drop in Pt reduction yield (to 60%) when employing Pd:Pt molar ratio lower than 7:3 (Table 1). Starting with Pd:Pt ratio lower than 5:5 resulted in very low yields, with no evident NPs dispersion formation. Moreover, pure Pt-MUA NPs could not be obtained by reduction of the Pt precursor under the conditions used in the CoRed route in the absence of K₂PdCl₄. These results suggest that Pt reduction is catalyzed by Pd NPs seeds formed *in-situ* upon addition of NaBH₄. From now on, the Pd–Pt-MUA NPs will be labeled using the *observed* molar ratio, approximated to the unit.

HAADF-STEM and EDS analysis on samples prepared by PreRed and CoRed methods confirmed the formation of Pd–Pt bi-metallic NPs, having diameters in the range of 1–3 nm and compositions statistically distributed around the observed ICP-AES values (Fig. 2 and 3). This was observed even in the PreRed route, in which pre-formed Pt NPs are present (Fig. 2), suggesting that Pd species are preferentially reduced on the surface of Pt NPs, rather than nucleate separately and produce pure Pd-MUA NPs. The CoRed NPs present a broader compositional distribution at lower Pd mol.% (Fig. 3). Nonetheless, for both the synthetic routes, ~75% of the NPs are in the compositional range of ± 5 mol.% Pd around the value observed by ICP-OES analysis. Such quite narrow compositional distribution and the similar size of the NPs allowed to study the effect of the NPs composition on catalytic performances in detail.

In order to elucidate the structure of the NPs in terms of alloying/segregation of Pd and Pt and to study sulfur-metal stabilization and bond formation, EXAFS analysis was carried out on the as-prepared NPs. Results from the analysis of the first coordination shell around the

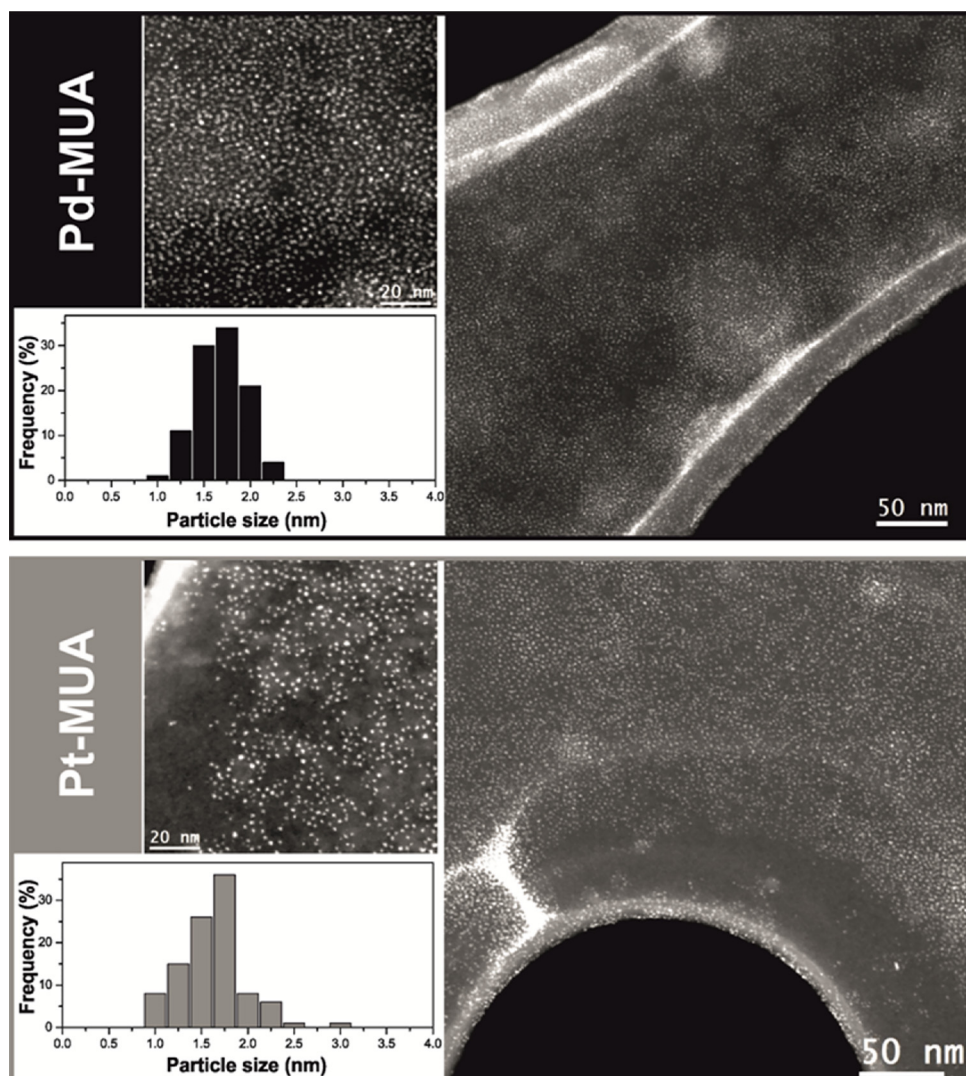


Fig. 1. TEM and NPs size distribution analysis results for pure Pd-MUA and Pt-MUA NPs samples. 400 nanoparticles were counted for obtaining NPs size distribution.

Table 1
ICP-OES results for Pd–Pt-MUA NPs dispersion prepared by CoRed route.

Expected Pd:Pt molar ratio	Observed Pd:Pt molar ratio (ICP-OES)	Pd yield (%)	Pt yield (%)	Average Pd:Pt molar ratio (EDS)
9:1	9.2:0.8	98	82	9.1:0.9
8:2	8.2:1.8	99	87	8.0:2.0
7:3	7.4:2.6	93	62	7.4:2.6
6:4	7.1:2.9	91	57	7.0:3.0
5:5	6.2:3.8	97	59	5.9:4.1

metal element for the pure Pd-MUA and Pt-MUA are reported in Table 2. The Pd-S and Pt-S contributions are at a distance typical of a binary sulfide (2.31 Å in PtS) [47] or a thiolate (2.27 Å for a Pt thiolate) [48] and indicate that about half of Pd and Pt are coordinated to a sulfur atom. Thiolate formation is expected from the synthesis in the presence of MUA, as previously reported by some of us [41], and it was corroborated by ¹H NMR results, showing broadened MUA ¹H signals in Pd–Pt-MUA samples (Fig. S1). Such a large molar fraction of Pd-S and Pt-s is consistent with ICP-OES results (metal:sulfur ratio of 0.5 ± 0.05, in agreement with nominal) and the dimension of the NPs (~2 nm), since roughly half of the atoms are in the outer atomic layer [49]. For the same reason, the Pd-Pd and Pt-Pt coordination numbers are very small. The Pt-Pt and Pd-Pd distances are quite shorter than the

corresponding bulk metals (2.75 Å for Pd-Pd and 2.77 Å for Pt-Pt), due to a strong contribution of surface atoms in particles smaller than 2 nm, as described in the literature for Pt [50], Pd [51] or Au [52] NPs.

Comparing CoRed and PreRed Pd–Pt NPs signals (Fig. 4, Table 3 and 4), the observed difference is striking. Table 3 reports the results of EXAFS fitting obtained for the first coordination shell around each metal element for CoRed samples (Fig. 4). The total coordination number of Pt, or Pd around each metal center is very similar to what found in Pt- and Pd-MUA. A minimum Pd content is necessary for the particles growth, but there is no sign that a Pd core is formed, the results highlights the formation of an alloy and as for the pure Pd- or Pt-MUA particles, a large fraction of thiolate. In all cases the bond lengths are close to those found on the pure Pd-MUA and Pt-MUA. These data suggest that, for the CoRed series, alloying of Pd and Pt occurs and both absorbers see similar amounts of each other and S. The distance contraction respect to bulk values has been already observed with EXAFS by Bazin et al., even if not fully commented [53] and by Bernardi et al. [54] as a function of Pd content. Our particles, though, exhibit much smaller sizes.

Results from the analysis of the first coordination shell around and Pt for the PreRed samples (Table 4) reveal a number of differences, indicating that Pd and S cover Pt clusters and that Pt remains at the core. Changes with respect to CoRed samples are most evident at Pt L₃ edge, being the average CN of Pt significantly larger. The average

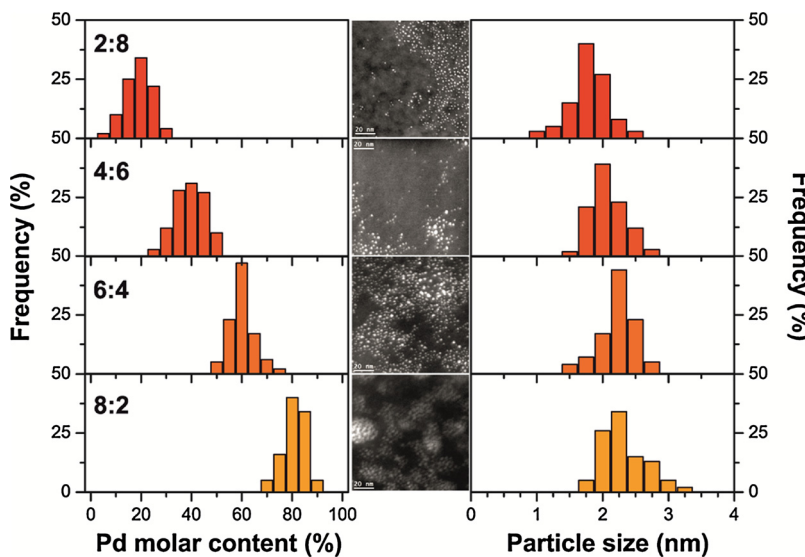


Fig. 2. TEM and single-particle EDS analysis results for selected PreRed Pd–Pt-MUA samples. Left: frequency with which a given Pd content is observed by single particle EDS over a certain Pd–Pt sample, having an *average* composition (observed by ICP) as indicated by the labels in the figure; center: representative HAADF-STEM images; right: NPs size distribution. 400 nanoparticles were counted for obtaining NPs size distribution.

coordination number is close to 5.4 that is possible for a core of Pt of 0.6 nm (cube octahedron of order $m = 2$, where $m = 1$ is a single atom). Moreover, much smaller Pt-S CNs were observed (half than in co-reduced samples), suggesting that a smaller fraction of Pt is exposed and/or that S preferentially binds to Pd. All the samples exhibit a Pd-S CN close to 2 as in the case of Pd-MUA and the co-reduced PdPt-MUA series, indicating that Pd should be at the outside of the cluster where S plays the role of protective layer. Accordingly, the Pd edge is sensitive to the presence of Pt in all samples, but not the other way around (Pt-Pd path not contained in the Pt L₃ EXAFS signal). This could be explained by a scenario in which Pd grows only on Pt cores (although some Pt is still uncovered) and a fraction (nearly half) of Pd is in the form of thiolate. The net coordination of Pd around Pt would be thus too small (< 1) to be reliably fitted.

3.2. NH_3BH_3 hydrolysis catalyzed by Pd–Pt-MUA NPs

The as-synthesized Pd–Pt-MUA NPs were transferred in aqueous NaOH solutions (Pd–Pt-MUATE NPs are formed, where MUATE stands for carboxylate form of MUA) and tested for H₂ production by AB catalytic hydrolysis (Fig. 5). Pt-MUATE and Pd-MUATE had very different initial H₂ production rates (~ 450 vs $100 \mu\text{mol H}_2 \text{ min}^{-1}$, respectively – inset of Fig. 5), and yielded total hydrolysis of AB after 30

and 120 min, respectively. The initial TOF values observed for Pd–Pt-MUATE NPs are intermediate between those of Pt and Pd (inset of Fig. 5). The values are normalized by moles of catalyst, since the number of active sites is not known. Since all the studied NPs have very similar size distribution (see Figs. 1–3), the differences observed in the TOF are mainly due to effects of particles surface composition and active sites accessibility.

Distinct activity was observed for CoRed and PreRed Pd₆Pt₄-MUATE NPs: the PreRed samples showed an initial rate 3 times higher than that of the CoRed samples, in a very reproducible way. This was not expected, basing on the Pt-core@Pd-shell structure of PreRed samples observed by EXAFS, which would point to a surface rich in less-active Pd. However, the low Pt-S CNs observed by EXAFS for Pt-MUA and PreRed samples compared to CoRed samples suggests that Pt is less passivated by S atoms in PreRed samples. Therefore, until complete coverage of the surface by Pd, the activity of the Pd–Pt-MUATE NPs remains similar to that of Pt. In Pd₈Pt₂-MUATE samples, which have higher Pd molar content, the surface of the NPs is almost completely composed of Pd irrespectively from the synthetic procedure, and the CoRed and PreRed samples behave very similarly. Notably, the reaction shows a rate (r_{AB}) which is first-order in AB concentration, in accordance with kinetic studies on Pt/CNTs [26], for which a Langmuir–Hinshelwood (L–H) mechanism was observed:

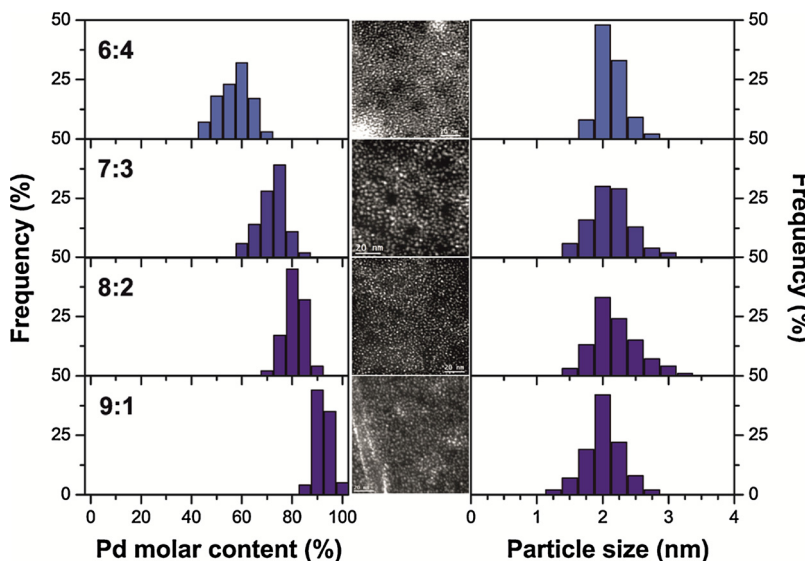


Fig. 3. TEM and single-particle EDS analysis results for CoRed Pd–Pt-MUA samples. Left: frequency with which a given Pd content is observed by single particle EDS over a certain Pd–Pt sample, having an *average* composition (observed by ICP) as indicated by the labels in the figure; center: representative HAADF-STEM images; right: NPs size distribution. 400 nanoparticles were counted for obtaining NPs size distribution.

Table 2

Results of EXAFS refinements on Pd-MUA and Pt-MUA particles. CN = coordination number; R = interatomic distance. Brackets report the standard deviation error on each parameter. See Table S2 for further details.

Pd-MUA	CN	R(Å)	Pt-MUA	CN	R(Å)
Pd–S	2.1(3)	2.30(1)	Pt–S	0.8(2)	2.28(1)
Pd–Pd	2.0(7)	2.74(1)	Pt–Pt	2.8(6)	2.73(1)

$$r_{AB} = k \theta_{AB} \theta_{H2O} \quad (3)$$

in which θ_{AB} and θ_{H2O} are respectively the coverage of NH_3BH_3 and water.

The average TOF (i.e. calculated over the entire hydrolysis time) for Pt-MUAt NPs was comparable to that of previously reported PVP-protected Pt NPs (100 vs 108 mol H_2 mol catalyst $^{-1}$ min $^{-1}$) [30]. However, here Pd–Pt NPs did not show higher TOF than Pt NPs, in contrast to what reported in ref. [30] (125 mol H_2 mol catalyst $^{-1}$ min $^{-1}$). This difference is probably due to the weaker interaction of PVP with the NPs surface compared to MUA, which results in more accessible active sites, but on the downside can yield to aggregation over time [30]. Consistently, Pd-MUAt NPs, which have higher Pd–S CNs, showed a two times lower activity with respect to PVP-protected NPs.

Despite this, the use of MUA as a protective ligand brings about advantages with respect to PVP, such as the ability to precipitate the NPs out of acidic aqueous solutions. In this way, the catalyst can be easily recovered and separated from the water-soluble reaction by-products by centrifugation. Following water washings, the NPs can be redispersed in the basic solution employed in AB hydrolysis, maintaining 90% of activity after 5 precipitation-redispersion cycles (Fig. S2). Notably, successive additions of AB to the reaction solution (without washing) led to a progressive deactivation of the catalyst due

Table 3

Results of EXAFS refinements on CoRed Pd–Pt-MUA NPs. CN = coordination number; R = interatomic distance. Brackets report the standard deviation error on each parameter. See Table S3 for further details.

	Pd	CN	R(Å)	Pt	CN	R(Å)
Pd_2Pt_8	Pd–S	2.2(2)	2.29(1)	Pt–S	2.1(2)	2.30(1)
	Pd–Pd	0.8(2)	2.68(2)	Pt–Pt	1.2(5)	2.73(2)
	Pd–Pt	1.3(4)	2.72(2)	Pt–Pd	0.9(4)	2.71(2)
Pd_7Pt_3	Pd–S	2.0(3)	2.29(1)	Pt–S	2.0(3)	2.30(1)
	Pd–Pd	1.0(3)	2.73(2)	Pt–Pt	0.7(3)	2.75(2)
	Pd–Pt	0.6(3)	2.74(2)	Pt–Pd	1.4(4)	2.73(1)
Pd_8Pt_2	Pd–S	1.8(2)	2.30(1)	Pt–S	2.0(3)	2.30(1)
	Pd–Pd	1.6(2)	2.74(1)	Pt–Pt	1.3(7)	2.72(2)
	Pd–Pt	1.0(3)	2.76(2)	Pt–Pd	1.4(4)	2.72(2)
Pd_9Pt_1	Pd–S	2.2(2)	2.30(1)	Pt–S	2.3(3)	2.30(1)
	Pd–Pd	2.1(3)	2.71(3)	Pt–Pt	1.5(5)	2.73(2)
	Pd–Pt	1.1(4)	2.73(3)	Pt–Pd	1.1(5)	2.71(1)

to poisoning by byproducts (no modification in NPs size was observed – Fig. S3), reaching less than 40% of activity after 5 additions (Fig. S2), in agreement with previous studies [30]. This approach is very interesting also in view of the recent studies of AB regeneration, which would require its efficient separation from the catalyst dispersion. Finally, unprotected Pt NPs (not functionalized by MUA), shown a slightly lower initial rate compared to Pt-MUAt NPs and visibly aggregated during the course of the experiment (Fig. S4). This further suggests that MUA functionalization favors Pt NPs dispersion, while maintaining exposed active sites, resulting in an overall increase of the H_2 production initial rate.

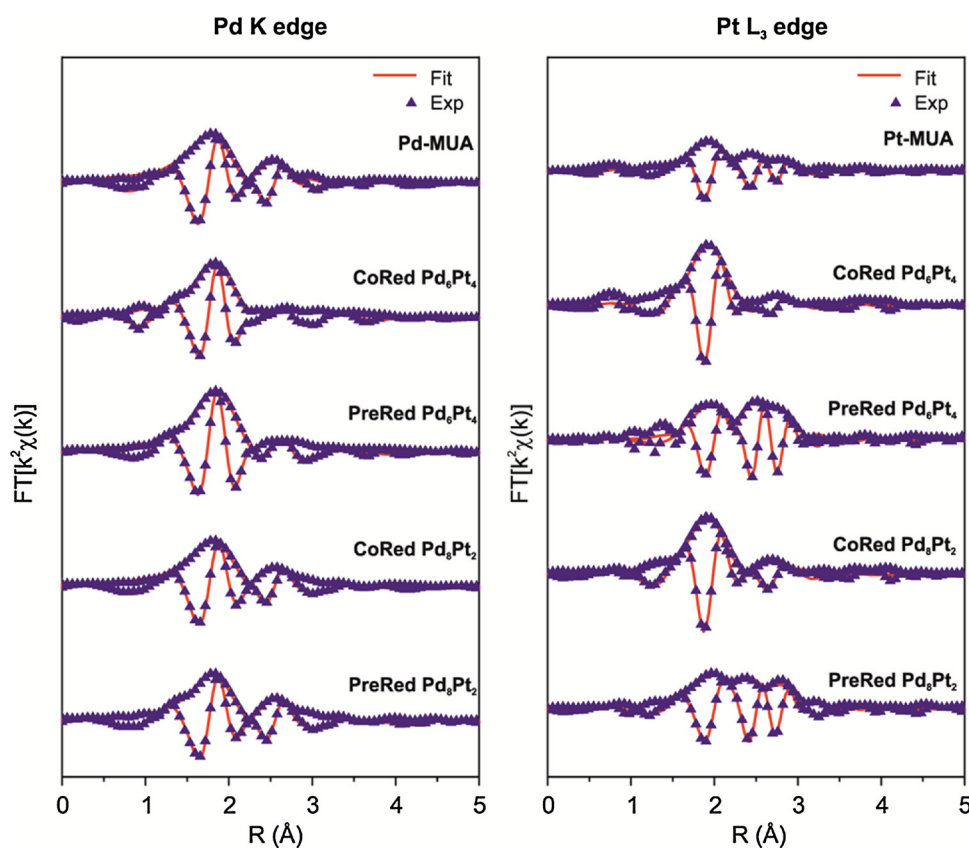


Fig. 4. Fourier transform of selected experimental (blue triangles) and simulated (red lines) EXAFS signals at Pd K and Pt L_3 edge, respectively. Pd:Pt molar ratios of 8:2 and 6:4 were selected to compare the structure of CoRed and PreRed NPs having similar composition. (For interpretation of the references to colour in this figure legend, the reader is referred to the web version of this article.)

Table 4

Results of EXAFS refinements on PreRed Pd–Pt-MUA NPs. CN = coordination number; R = interatomic distance. Brackets report the standard deviation error on each parameter. See Table S4 for further details.

	Pd	CN	R(Å)	Pt	CN	R(Å)
Pd ₂ Pt ₈	Pd–S	1.7(4)	2.30(1)	Pt–S	0.6(2)	2.30(1)
	Pd–Pd	1.5(4)	2.73(2)	Pt–Pt	5.1(4)	2.75(1)
	Pd–Pt	2.0(5)	2.74(2)			
Pd ₄ Pt ₆	Pd–S	2.2(3)	2.30(1)	Pt–S	0.7(2)	2.30(1)
	Pd–Pd	1.2(4)	2.70(2)	Pt–Pt	6.1(9)	2.75(1)
	Pd–Pt	1.7(5)	2.72(3)			
Pd ₆ Pt ₄	Pd–S	1.9(4)	2.30(1)	Pt–S	1.0(2)	2.30(1)
	Pd–Pd	2.0(4)	2.73(1)	Pt–Pt	4.2(4)	2.73(1)
	Pd–Pt	1.3(7)	2.77(3)			
Pd ₈ Pt ₂	Pd–S	1.6(3)	2.29(1)	Pt–S	0.9(4)	2.31(2)
	Pd–Pd	1.9(4)	2.75(1)	Pt–Pt	5.6(4)	2.73(1)
	Pd–Pt	0.9(5)	2.77(3)			

3.3. Pd–Pt@CeO₂/Si-Al₂O₃ characterization

Physisorption and chemisorption experiments on Pd–Pt@CeO₂/Si-Al₂O₃ catalysts calcined at 500 °C revealed that all the supported samples had similar surface areas, pore-size distributions, and active phase accessibility, as detailed in Table S1. The results for pure Pd and Pt NPs are comparable with those reported in previous studies on similar materials, and the accessibility of bi-metallic Pd–Pt NPs is consistently similar [55–57]. This is in accordance with TEM/EDS and EXAFS results on supported Pd–Pt@CeO₂-based catalysts (*vide infra*).

TEM/EDS analysis of the Pd–Pt@CeO₂/Si-Al₂O₃ samples revealed the presence of small nanoparticles of 1–5 nm in size, forming a uniform layer on the Si-Al₂O₃ support (Fig. 6, top). The Pd:Pt atomic ratio observed by EDS (Fig. 6, bottom) is as expected and consistent with ICP-OES results of the pristine NPs. Ce and Pd–Pt signals were almost always associated, except for a small fraction of stand-alone CeO₂ NPs, in agreement with the formation of Pd–Pt@CeO₂ entities with core-shell morphology deposited on the silanized alumina - which after

calcination yields a inhomogeneous thin silica overlayer on alumina [58].

Selected supported Pd–Pt@CeO₂/Si-Al₂O₃ samples were analyzed by *in-situ* EXAFS in order to get insight in the evolution of Pd and Pt chemical state and of the structure of the active phase NPs during thermal treatments under oxidizing and reducing conditions. PreRed Pd₆Pt₄@CeO₂ and CoRed Pd₆Pt₄@CeO₂-based samples were selected since the bare NPs revealed the most different structure and catalytic performances in AB hydrolysis (See Section 3.1 and 3.2). Very interestingly, after oxidation and reduction treatments, the results of EXAFS refinement for PreRed and CoRed samples are numerically equivalent (Tables 5 and 6). A re-organization of the NPs occurred, which was not dependent on the NPs synthetic route (PreRed or CoRed).

Pd K edge and Pt L₃ edge *in-situ* EXAFS signals of the fresh (*i.e.* not calcined), 250 °C-oxidized and 250 °C-reduced PreRed Pd₆Pt₄@CeO₂ and CoRed Pd₆Pt₄@CeO₂ samples are reported in Fig. 7. In the fresh CoRed Pd₆Pt₄@CeO₂ sample, about half of Pd and Pt atoms are coordinated to S (Table 5). Both Pt and Pd have similar environments and there is no indication of Pd/Pt segregation. The oxidation step to 250 °C results in an increase of dispersion or disorder of the pristine particles. Most sulfur is removed, though a small Pt–S contribution remains; Pt–Pt metallic bonds are formed, while Pd–Pd and Pt–Pd disappear due to oxidation of Pd and formation of Pd–O bonds, indicating that Pd is easier to oxidize and more exposed at the gas interface. The successive reduction step (5% H₂/Ar, 250 °C) results in the segregation of the two metals: Pt is surrounded by a majority of Pt and Pd by a majority of Pd.

The core-shell picture in which the majority of Pd is located on a thin shell justifies the results: Pd migrates at the surface and it is partially oxidized, it coordinates to other Pd and (in part) to Pt, while the majority of Pt is in a more coordinated environment at the core of the particle. The tendency to segregate Pd at the surface of the cluster is in agreement with previous findings of Bazin et al. [53] and Bernardi et al. [54]. It is possible to relate the CN of Pt to the size of the core of the particle [49,59,60], that is close to 1.2 nm. Considering the EXAFS estimate for the Pt–Pt, Pd–Pt, Pd–Pd bond lengths, the whole cluster should have an average diameter of 1.6 nm. In the hypothesis of a cuboctahedron (Fig. 8), if the edge length is m, m = 1 corresponds to an isolated atom, m = 2 corresponds to a cluster made of 13 atoms, one of which is at the core and 12 around like in a fcc crystal structure. The

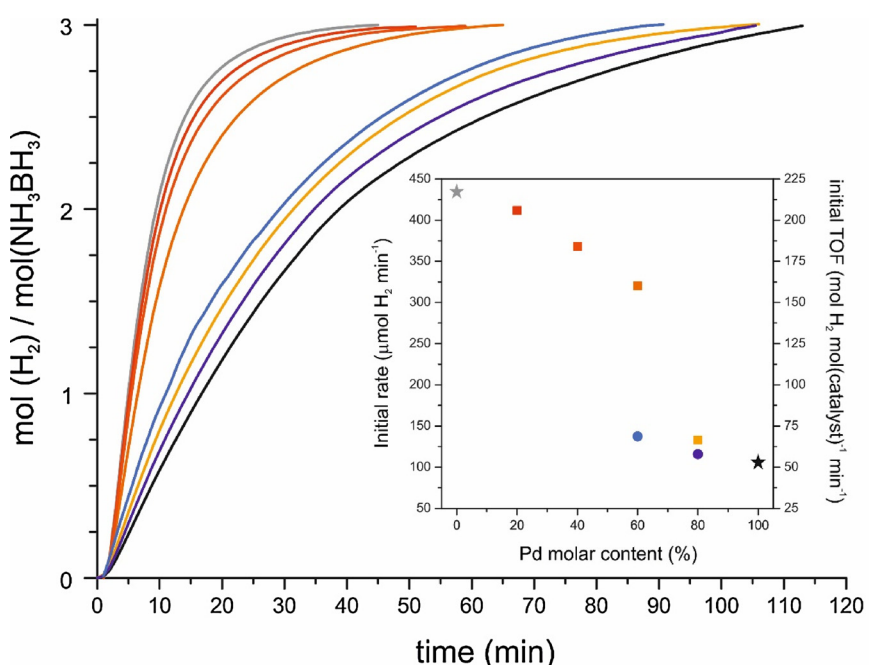


Fig. 5. Production of H₂ by NH₃BH₃ (AB) hydrolysis catalyzed by Pd-MUATE, Pt-MUATE and selected Pd–Pt-MUATE NPs. Inset: the initial rates of H₂ production, extrapolated from the linear part of the curve, and the corresponding turn over frequency (TOF) calculated basing on the moles of catalyst. Conditions: NaOH concentration = 100 mM; metals/AB molar ratio = 0.001; T = 20 °C. Blank experiments without catalyst did not show any H₂ evolution.

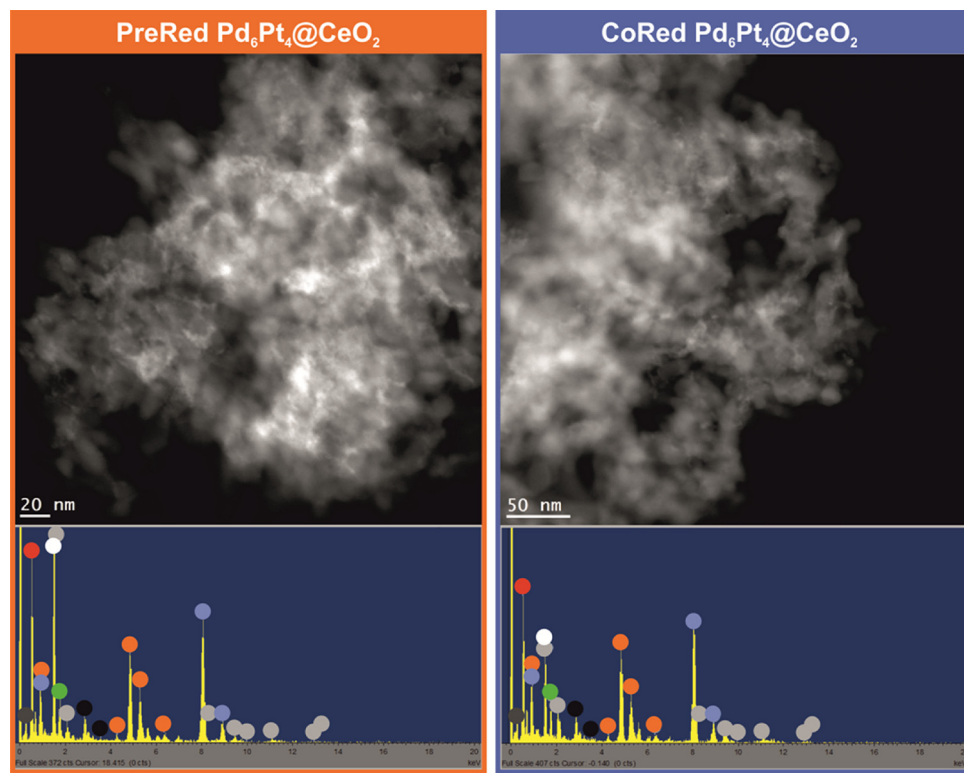


Fig. 6. Representative TEM images (top) and EDS analysis (bottom) of fresh CoRed and PreRed $\text{Pd}_6\text{Pt}_4@\text{CeO}_2/\text{Si-Al}_2\text{O}_3$ samples. EDS signals: Pd (black), Pt (light grey), Ce (orange), O (red), Al (white), Si (green), C (dark grey), Cu (from the grid – light blue). (For interpretation of the references to colour in this figure legend, the reader is referred to the web version of this article.)

Table 5

Results of in-situ EXAFS refinements on particles grown starting from CoRed Pd–Pt-MUA NPs. CN = coordination number; R = interatomic distance. Brackets report the standard deviation error on each parameter. See Table S5 for further details.

	Pd	CN	R(Å)	Pt	CN	R(Å)
Pd_6Pt_4						
Pd–S	2.2(2)	2.29(1)	Pt–S	2.1(2)	2.30(1)	
Pd–Pd	0.8(2)	2.68(2)	Pt–Pt	1.2(5)	2.73(2)	
Pd–Pt	1.3(4)	2.72(2)	Pt–Pd	0.9(4)	2.71(2)	
Pd_6Pt_4 Oxidized						
Pd–O	2.5(4)	2.03(1)	Pt–O	1.5(3)	1.99(2)	
			Pt–S	0.4(3)	2.28(3)	
			Pt–Pt	3.0(8)	2.76(1)	
Pd_6Pt_4 Reduced						
Pd–O	1.0(3)	2.03(1)				
Pd–Pd	2.1(4)	2.72(1)	Pt–Pt	6.2(9)	2.73(1)	
Pd–Pt	1.5(3)	2.70(2)	Pt–Pd	1.6(3)	2.67(1)	

number of atoms in a cuboctahedron follows the formula $n(m) = 10/3 \text{ m}^3 - 5 \text{ m}^2 + 11/3 \text{ m} - 1$ [61]; our average cluster should have a core with an edge length close to 3 (depicted in white in Fig. 8). The outer sphere of such cluster (the $m = 4$ shell) contains 63% of the total number of atoms, which corresponds to the fraction of Pd in the sample. This reasoning is based on one particular (and most probable) fcc cluster geometry, but the estimate holds for icosahedral clusters or similar shapes which cannot be distinguished without information on second neighbors, too difficult to precisely detect in these samples [60].

The fresh PreRed $\text{Pd}_6\text{Pt}_4@\text{CeO}_2$ sample already exhibits a Pd@Pt core-shell structure, with S coordinated preferentially to Pd (Table 6). The oxidation step completely removes the sulfur protection from Pt and a Pt-Pd path appears, indicating that at this step the oxidation reaches the particle core, forming not only a part of Pt oxide, but promoting a partial alloying of Pd and Pt, too. The successive reduction step produces the same effects as for CoRed: a Pt rich core is formed covered by metallic Pd, since a Pt-Pd contribution is in evident contrast

Table 6

Results of in-situ EXAFS refinements on particles grown starting from PreRed Pd–Pt-MUA NPs. CN = coordination number; R = interatomic distance. Brackets report the standard deviation error on each parameter. See Table S6 for further details.

	Pd	CN	R(Å)	Pt	CN	R(Å)
Pd_6Pt_4						
Pd–S	1.9(4)	2.30(1)	Pt–S	1.0(2)	2.30(1)	
Pd–Pd	2.0(4)	2.73(1)	Pt–Pt	4.2(4)	2.73(1)	
Pd–Pt	1.3(7)	2.77(3)				
Pd_6Pt_4 Oxidized						
Pd–O	3.6(7)	2.02(2)	Pt–O	2.5(8)	2.03(2)	
Pd–Pd	0.4(2)	2.69(2)	Pt–Pt	1.4(4)	2.74(2)	
Pd–Pt	0.7(3)	2.73(2)	Pt–Pd	0.6(2)	2.73(2)	
Pd_6Pt_4 Reduced						
Pd–O	1.0(1)	2.04(1)				
Pd–Pd	1.7(3)	2.73(1)	Pt–Pt	5.9(7)	2.70(1)	
Pd–Pt	2.0(2)	2.73(1)	Pt–Pd	1.5(2)	2.68(1)	

with the initial PreRed. The very same considerations applied to CoRed-reduced can be made.

3.4. Water gas shift reaction over Pd–Pt@ $\text{CeO}_2/\text{Si-Al}_2\text{O}_3$

Selected Pd–Pt@ $\text{CeO}_2/\text{Si-Al}_2\text{O}_3$ catalysts were tested in the WGSR, in order to determine the effect of NPs composition on the activity, and in particular if bimetallic catalysts would show a cooperative effect, leading to enhancement of the performance. The samples and the pre-treatments conditions were selected to be consistent with the ones employed in the EXAFS study. The steady state CO conversion during WGSR experiments at 250 °C over 250 °C-pre-oxidized, or pre-reduced catalysts is shown in Fig. 9A and B, respectively. Pt@ CeO_2 -based catalysts were the most active and stable in both cases, and their activity was not affected by the pre-treatment conditions. On the other hand, pre-oxidized Pd@ CeO_2 -based catalysts showed very low activity and underwent fast deactivation at 250 °C, in accordance with previously

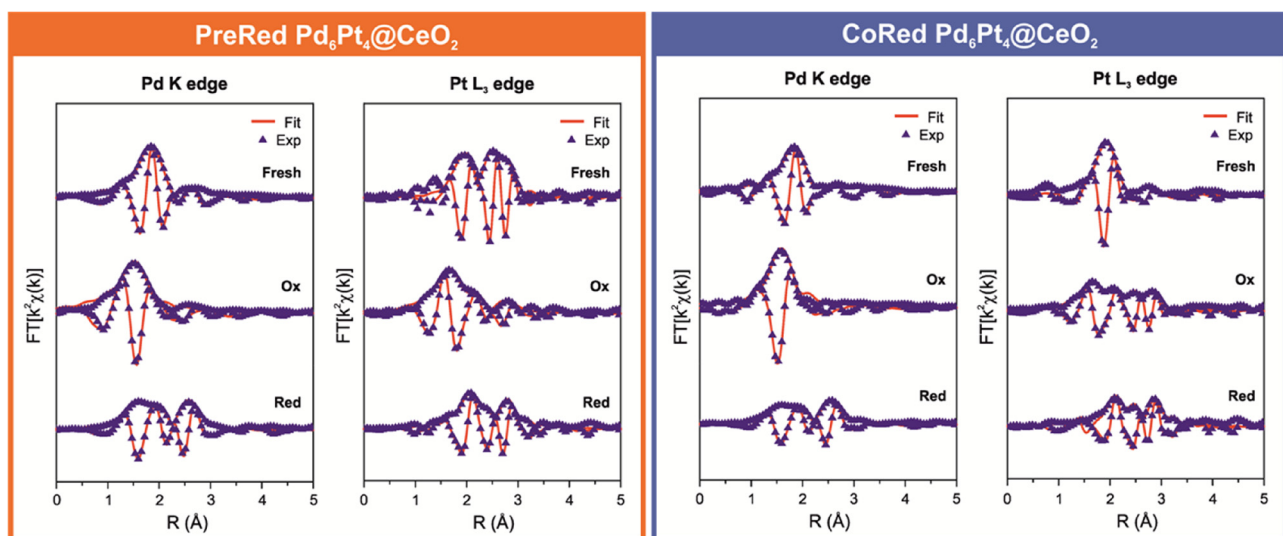


Fig. 7. Fourier Transforms of experimental data and fits of CoRed and PreRed Pd₆Pt₄@CeO₂ samples supported on Si-Al₂O₃ after different thermo-chemical treatments.

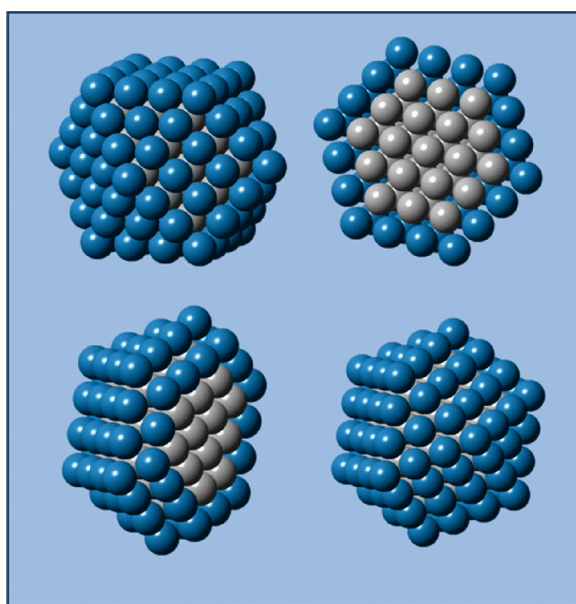


Fig. 8. Idealized view of a $m = 4$ cuboctahedron with a $m = 3$ Pt core and a Pd outer shell (Pd: blue; Pt: grey). (For interpretation of the references to colour in this figure legend, the reader is referred to the web version of this article.)

reported result on similar catalysts, due to strong metal-support interactions (SMSI) such as electron transfer effects or encapsulation of Pd by partially reduced CeO_{2-x} [33]. Moreover, pre-reduction led to almost complete deactivation of the catalyst, in contrast with Pt@CeO₂-based catalysts, suggesting that SMSI with CeO_{2-x} mainly affects the activity of Pd-based systems. Interestingly, encapsulated Pt@CeO₂ was reported to be active for WGSR, due to electron transfer from Pt to Ce, evidenced from a blue shift of the absorption edge (O_{2p}–Ce_{4f}) of the n-type semiconductive ceria in diffuse UV reflectance experiments [62]. These observations open up interesting questions for future systematic and mechanistic studies about metal-ceria interaction in WGSR.

The observed conversion values over PreRed and CoRed Pd₆Pt₄@CeO₂-based catalysts were intermediate between those of pure Pt- and Pd-based catalysts, evidencing that cooperative effects are not in play under the conditions employed in this study. The catalysts slightly deactivated over time, consistently with a deactivation of Pd and with a residual activity after 2 h mostly due to Pt, further

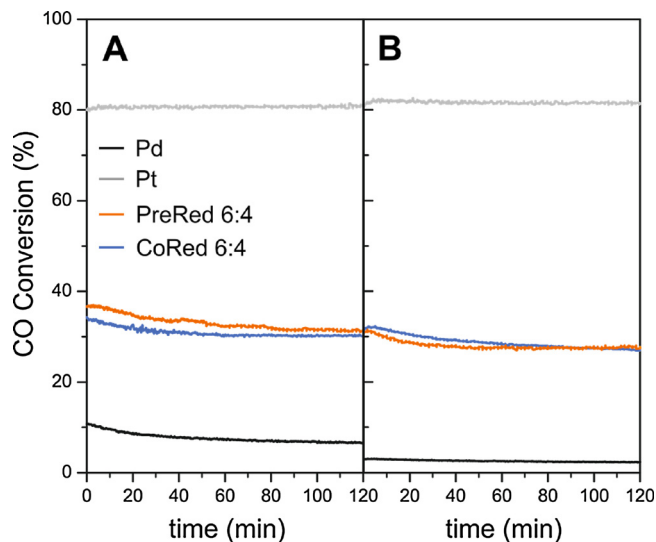


Fig. 9. Steady state WGSR experiments at 250 °C over Pd@CeO₂/Si-Al₂O₃, Pt@CeO₂/Si-Al₂O₃ and selected Pd–Pt@CeO₂/Si-Al₂O₃ catalysts, pretreated (A) at 250 °C in O₂(5%)/Ar and (B) at 250 °C in H₂(5%)/Ar. Conditions: 7.6 Torr CO, 38 Torr H₂O, Ar balance, GHSV = 75,000 h⁻¹.

suggesting that Pd-Ce SMSI are the reason of deactivation. Interestingly, PreRed and CoRed Pd₆Pt₄@CeO₂-based catalysts showed comparable conversion trends, in stark contrast with what observed in AB catalytic hydrolysis experiments (Fig. 5), consistently with the change of structure in the NPs observed by EXAFS (*vide supra*).

In order to further explore the effect of the active phase composition on the WGSR performance, light-off experiments were performed on a wider array of Pd–Pt@CeO₂-based samples (Fig. 10). Also in this case, PreRed and CoRed samples showed comparable light-off curves, and the activity trend was linearly dependent on the composition with no considerable cooperative effects, as visualized by the trend in temperature at which the WGS chemical equilibrium is achieved (T_{EQ}) in the inset of Fig. 10. In all cases, the selectivity to H₂ and CO₂ was 100%. No methane production was observed during the catalytic tests, as confirmed also by analysis of the reaction products by GC equipped with a FID detector.

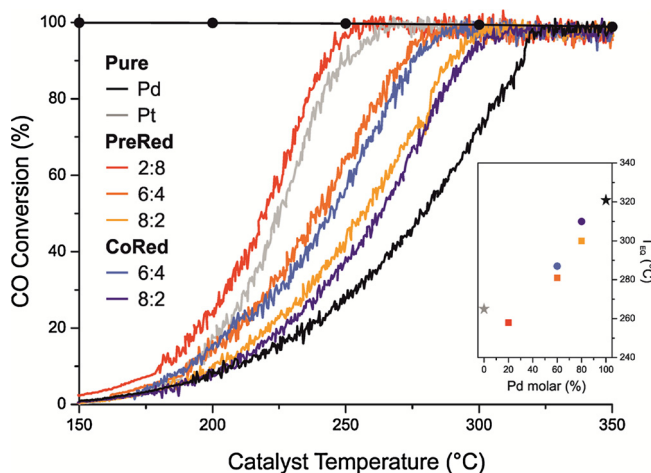


Fig. 10. WGSR light-off experiments over $\text{Pd}@\text{CeO}_2/\text{Si-Al}_2\text{O}_3$, $\text{Pt}@\text{CeO}_2/\text{Si-Al}_2\text{O}_3$ and selected $\text{Pd-Pt}@\text{CeO}_2/\text{Si-Al}_2\text{O}_3$ catalysts calcined at 500°C in air. Dots in the graph indicate CO conversion values at the thermodynamic equilibrium. Inset: temperature at which the WGS chemical equilibrium is achieved (T_{EQ}) versus Pd mol.%. Conditions: 7.6 Torr CO, 38 Torr H_2O , Ar balance, GHSV = $75,000 \text{ h}^{-1}$, 2°C min^{-1} heating rate.

4. Conclusions

In conclusion, we have developed wet-chemistry methods to synthesize small (1.5–2.5 nm) and functionalized Pd–Pt NPs with tunable structure (alloy or core-shell) and composition, as indicated by TEM, EDS mapping and EXAFS analysis. Aminoborane hydrolysis was used as a model reaction to investigate the activity trend of the as-synthesized Pd–Pt NPs. In this case, the activity of the NPs was dependent on the synthetic route (CoRed or PreRed), since it was influenced by the extent of surface coordination by MUA, rather than the Pd:Pt molar ratio, as demonstrated by the different activity of PreRed and CoRed $\text{Pd}_6\text{Pt}_4\text{-MUAte}$ samples. While presenting some drawbacks related to partial blocking of active sites, NPs functionalization with MUA can be exploited both to separate the catalyst dispersion from the reaction mixture (by precipitation driven by acidification) and to synthesize well-defined, active and stable nanostructured Pd–Pt@ CeO_2 -based catalysts by a previously reported self-assembly route [41]. Applying similar strategies to base-base metal systems could yield even better noble metal-free catalysts, possibly showing performances comparable to noble metals. While thiol-stabilized base metal alloys nanoparticles are neither easily synthesized nor water-stable, other methods to obtain precisely controlled NPs can be employed (e.g. solvothermal synthesis [44]).

The supported Pd–Pt@ $\text{CeO}_2/\text{Si-Al}_2\text{O}_3$ catalysts based on NPs prepared by CoRed or PreRed showed similar WGSR performances, intermediate between those of $\text{Pd}@\text{CeO}_2$ and $\text{Pt}@\text{CeO}_2$ -based catalysts. EXAFS analysis revealed that, regardless of the synthetic route, the NPs underwent a similar modification during oxidation and reduction, leading to the formation of Pt-rich core@Pd–Pt-shell under reducing conditions. Notably, no cooperative effects were observed for the Pd–Pt-based systems studied herein, in accordance with recent reports on well-defined nanostructured Pd–Pt materials [3]. This suggests that cooperative effects observed on traditionally-prepared bimetallic catalysts may result from other, more subtle properties of the materials, such as change in active phase dispersion and accessibility. All considered, this work provides new insights in the synthesis and characterization of more active and stable Pd–Pt catalysts and demonstrates that well-defined bimetallic catalysts can be used as model to elucidate structure-activity and -stability relationships.

Acknowledgements

M.M., T.M., G.A., M.C. and P.F. acknowledge financial support from University of Trieste through the FRA2015 project. J.J.D. would like to acknowledge the financial support of MINECO (Ramon y Cajal Program and ENE2017-82451 project).

Appendix A. Supplementary data

Supplementary material related to this article can be found, in the online version, at doi:<https://doi.org/10.1016/j.apcatb.2018.05.019>.

References

- [1] R. Ghosh Chaudhuri, S. Paria, Core/shell nanoparticles: classes, properties, synthesis mechanisms, characterization, and applications, *Chem. Rev.* 112 (2012) 2373–2433, <http://dx.doi.org/10.1021/cr100449n>.
- [2] M. Cargnello, V.V.T. Doan-Nguyen, T.R. Gordon, R.E. Diaz, E.A. Stach, R.J. Gorte, P. Fornasiero, C.B. Murray, Control of metal nanocrystal size reveals metal-support interface role for ceria catalysts, *Science* (80-) 341 (2013) 771–773, <http://dx.doi.org/10.1126/science.1240148>.
- [3] E.D. Goodman, S. Dai, A.-C. Yang, C.J. Wrasman, A. Gallo, S.R. Bare, A.S. Hoffman, T.F. Jaramillo, G.W. Graham, X. Pan, M. Cargnello, Uniform Pt/Pd bimetallic nanocrystals demonstrate platinum effect on palladium methane combustion activity and stability, *ACS Catal.* 7 (2017) 4372–4380, <http://dx.doi.org/10.1021/acscatal.7b00393>.
- [4] J. Luo, M. Monai, C. Wang, J.D. Lee, T. Duchon, F. Dvorak, V. Matolin, C.B. Murray, P. Fornasiero, R.J. Gorte, T. Duchoň, F. Dvořák, V. Matolín, C.B. Murray, P. Fornasiero, R.J. Gorte, Unraveling the surface state and composition of highly selective nanocrystalline Ni-Cu alloy catalysts for hydrodeoxygenation of HMF, *Catal. Sci. Technol.* 7 (2017) 1735–1743, <http://dx.doi.org/10.1039/C6CY02647H>.
- [5] J. Luo, H. Yun, A.V. Mironenko, K. Goulas, J.D. Lee, M. Monai, C. Wang, V. Vorotnikov, C.B. Murray, D.G. VLachos, P. Fornasiero, R.J. Gorte, Mechanisms for high selectivity in the hydrodeoxygenation of 5-hydroxymethylfurfural over PtCo nanocrystals, *ACS Catal.* 6 (2016) 4095–4104, <http://dx.doi.org/10.1021/acscatal.6b00750>.
- [6] K. Persson, K. Jansson, S. Jaras, Characterisation and microstructure of Pd and bimetallic Pd–Pt catalysts during methane oxidation, *J. Catal.* 245 (2007) 401–414, <http://dx.doi.org/10.1016/j.jcat.2006.10.029>.
- [7] T. Fujikawa, K. Tsuji, H. Mizuguchi, H. Godo, K. Idei, K. Usui, EXAFS characterization of bimetallic Pt–Pd/SiO₂–Al₂O₃ catalysts for hydrogenation of aromatics in diesel fuel, *Catal. Letters.* 63 (1999) 27–33, <http://dx.doi.org/10.1023/A:1019008803028>.
- [8] C. Micheaud-Espécel, D. Bazin, M. Guérin, P. Marécot, J. Barbier, Study of supported bimetallic Pd–Pt catalysts. Characterization and catalytic activity for toluene hydrogenation, *React. Kinet. Catal. Lett.* 69 (2000) 209–216, <http://dx.doi.org/10.1023/A:1005623127174>.
- [9] T. Kabe, W. Qian, Y. Hirai, L. Li, A. Ishihara, Hydrodesulfurization and hydrogenation reactions on noble metal catalysts, *J. Catal.* 190 (2000) 191–198, <http://dx.doi.org/10.1006/jcat.1999.2742>.
- [10] M. Khan, A. Bin Yousaf, M. Chen, C. Wei, X. Wu, N. Huang, Z. Qi, L. Li, Mixed-phase Pd–Pt bimetallic alloy on graphene oxide with high activity for electrocatalytic applications, *J. Power Sources* 282 (2015) 520–528, <http://dx.doi.org/10.1016/j.jpowsour.2015.02.090>.
- [11] B. Lim, M. Jiang, P.H.C. Camargo, E.C. Cho, J. Tao, X. Lu, Y. Zhu, Y. Xia, Pd–Pt bimetallic nanodendrites with High activity for oxygen reduction, *Science* (80-) 324 (2009) 1302–1305 <http://science.sciencemag.org/content/324/5932/1302.abstract>.
- [12] M.A. Hoque, S. Lee, N.-K. Park, K. Kim, Pd–Pt bimetallic catalysts for combustion of SOFC stack flue gas, *Catal. Today* 185 (2012) 66–72, <http://dx.doi.org/10.1016/j.cattod.2011.08.023>.
- [13] K. Persson, A. Ersson, S. Colussi, A. Trovarelli, S.G. Järås, Catalytic combustion of methane over bimetallic Pd–Pt catalysts: the influence of support materials, *Appl. Catal. B: Environ.* 66 (2006) 175–185, <http://dx.doi.org/10.1016/j.apcatb.2006.03.010>.
- [14] G. Corro, C. Cano, J.L.G. Fierro, A study of Pt–Pd/ γ -Al₂O₃ catalysts for methane oxidation resistant to deactivation by sulfur poisoning, *J. Mol. Catal. A: Chem.* 315 (2010) 35–42, <http://dx.doi.org/10.1016/j.molcata.2009.08.023>.
- [15] K. Narui, H. Yata, K. Furuta, A. Nishida, Effects of addition of Pt to PdO/Al₂O₃ catalyst on catalytic activity for methane combustion and TEM observations of supported particles, *Appl. Catal. A: Gen.* 179 (1999) (Accessed 30 October 2012), <http://www.sciencedirect.com/science/article/pii/S0926860X98003068>.
- [16] J. Luo, J.D. Lee, H. Yun, C. Wang, M. Monai, C.B. Murray, P. Fornasiero, R.J. Gorte, Base metal–Pt alloys: a general route to high selectivity and stability in the production of biofuels from HMF, *Appl. Catal. B: Environ.* 199 (2016) 439–446, <http://dx.doi.org/10.1016/j.apcatb.2016.06.051>.
- [17] M. Cargnello, T. Montini, S. Polizzi, N.L. Wieder, R.J. Gorte, M. Graziani, P. Fornasiero, Novel embedded Pd@CeO₂ catalysts: a way to active and stable catalysts, *Dalt. Trans.* 39 (2010) 2122–2127, <http://dx.doi.org/10.1039/B916035C>.
- [18] M. Cargnello, J.J.D. Jaen, J.C.H. Garrido, K. Bakhmutsky, T. Montini, J.J.C. Gamez,

- R.J. Gorte, P. Fornasiero, Exceptional activity for methane combustion over modular Pd@CeO₂ subunits on functionalized Al2O3, *Science* (80-) 337 (2012) 713–717, <http://dx.doi.org/10.1126/science.1222887>.
- [19] M. Melchionna, A. Beltram, T. Montini, M. Monai, L. Nasi, P. Fornasiero, M. Prato, Highly efficient hydrogen production through ethanol photoreforming by a carbon nanocone/Pd@TiO₂ hybrid catalyst, *Chem. Commun.* 52 (2016) 764–767, <http://dx.doi.org/10.1039/C5CC08015K>.
- [20] L.E. Marbella, D.M. Chevrier, P.D. Tancini, O. Shobayo, A.M. Smith, K.A. Johnston, C.M. Andolina, P. Zhang, G. Mpourmpakis, J.E. Millstone, Description and role of bimetallic prenucleation species in the formation of small nanoparticle alloys, *J. Am. Chem. Soc.* 137 (2015) 15852–15858, <http://dx.doi.org/10.1021/jacs.5b10124>.
- [21] B.L. Davis, D.A. Dixon, E.B. Garner, J.C. Gordon, M.H. Matus, B. Scott, F.H. Stephens, Efficient regeneration of partially spent ammonia borane fuel, *Angew. Chem. Int. Ed.* 48 (2009) 6812–6816, <http://dx.doi.org/10.1002/anie.200900680>.
- [22] F.H. Stephens, V. Pons, R. Tom Baker, Ammonia–borane: the hydrogen source par excellence? *Dalt. Trans.* (2007) 2613–2626, <http://dx.doi.org/10.1039/B70305C>.
- [23] A. Staubitz, A.P.M. Robertson, I. Manners, Ammonia–Borane and related compounds as dihydrogen sources, *Chem. Rev.* 110 (2010) 4079–4124, <http://dx.doi.org/10.1021/cr100088b>.
- [24] Ö. Metin, S. Duman, M. Dinç, S. Özkar, Oleylamine-Stabilized palladium(0) nanoclusters as highly active heterogeneous catalyst for the dehydrogenation of ammonia borane, *J. Phys. Chem. C* 115 (2011) 10736–10743, <http://dx.doi.org/10.1021/jp201906n>.
- [25] W. Chen, D. Li, C. Peng, G. Qian, X. Duan, D. Chen, X. Zhou, Mechanistic and kinetic insights into the Pt–Ru synergy during hydrogen generation from ammonia borane over PtRu/CNT nanocatalysts, *J. Catal.* 356 (2017) 186–196, <http://dx.doi.org/10.1016/j.jcat.2017.10.016>.
- [26] W. Chen, D. Li, Z. Wang, G. Qian, Z. Sui, X. Duan, X. Zhou, I. Yeboah, D. Chen, Reaction mechanism and kinetics for hydrolytic dehydrogenation of ammonia borane on a Pt/CNT catalyst, *AIChE J.* 63 (2017) 60–65, <http://dx.doi.org/10.1002/ai.15389>.
- [27] T. Kamegawa, T. Nakae, Complete hydrogen release from aqueous ammonia–borane over a platinum-loaded titanium dioxide photocatalyst, *Chem. Commun.* 51 (2015) 16802–16805, <http://dx.doi.org/10.1039/C5CC06639E>.
- [28] M. Rakap, Hydrolysis of sodium borohydride and ammonia borane for hydrogen generation using highly efficient poly(N-vinyl-2-pyrrolidone)-stabilized Ru–Pd nanoparticles as catalysts, *Int. J. Green. Energy* 12 (2015) 1288–1300, <http://dx.doi.org/10.1080/15435075.2014.895737>.
- [29] M. Rakap, Hydrogen generation from hydrolysis of ammonia borane in the presence of highly efficient poly(N-vinyl-2-pyrrolidone)-protected platinum–ruthenium nanoparticles, *Appl. Catal. A: Gen.* 478 (2014) 15–20, <http://dx.doi.org/10.1016/j.apcata.2014.03.022>.
- [30] M. Rakap, Poly(N-vinyl-2-pyrrolidone)-stabilized palladium–platinum nanoparticles-catalyzed hydrolysis of ammonia borane for hydrogen generation, *J. Power Sources* 276 (2015) 320–327, <http://dx.doi.org/10.1016/j.jpowsour.2014.11.146>.
- [31] J.-M. Yan, X.-B. Zhang, H. Shioyama, Q. Xu, Room temperature hydrolytic dehydrogenation of ammonia borane catalyzed by Co nanoparticles, *J. Power Sources* 195 (2010) 1091–1094, <http://dx.doi.org/10.1016/j.jpowsour.2009.08.067>.
- [32] T. Umegaki, J.-M. Yan, X.-B. Zhang, H. Shioyama, N. Kuriyama, Q. Xu, Preparation and catalysis of poly(N-vinyl-2-pyrrolidone) (PVP) stabilized nickel catalyst for hydrolytic dehydrogenation of ammonia borane, *Int. J. Hydrogen Energy* 34 (2009) 3816–3822, <http://dx.doi.org/10.1016/j.ijhydene.2009.03.003>.
- [33] N.L. Wieder, M. Cargnello, K. Bakhtmutsky, T. Montini, P. Fornasiero, R.J. Gorte, Study of the water-gas-shift reaction on Pd@CeO₂/Al2O3 core–shell catalysts, *J. Phys. Chem. C* 115 (2011) 915–919, <http://dx.doi.org/10.1021/jp102965e>.
- [34] T.L. LeValley, A.R. Richard, M. Fan, The progress in water gas shift and steam reforming hydrogen production technologies—a review, *Int. J. Hydrogen Energy* 39 (2014) 16983–17000, <http://dx.doi.org/10.1016/j.ijhydene.2014.08.041>.
- [35] T. Bunluesin, R.J. Gorte, G.W. Graham, Studies of the water-gas-shift reaction on ceria-supported Pt, Pd, and Rh: implications for oxygen-storage properties, *Appl. Catal. B: Environ.* 15 (1998) 107–114, [http://dx.doi.org/10.1016/S0926-3373\(97\)00040-4](http://dx.doi.org/10.1016/S0926-3373(97)00040-4).
- [36] L. Bobrova, D. Andreev, E. Ivanov, N. Mezentseva, M. Simonov, L. Makarshin, A. Gribovskii, V. Sadykov, Water–gas shift reaction over Ni/CeO₂ catalysts, *Catalysts*, 7 (2017).
- [37] A.M. Abdel-Mageed, G. Kučerová, J. Bansmann, R.J. Behm, Active Au species during the low-temperature water gas shift reaction on Au/CeO₂: a time-resolved operando XAS and DRIFTS study, *ACS Catal.* 7 (2017) 6471–6484, <http://dx.doi.org/10.1021/acscatal.7b01563>.
- [38] D. Vovchok, C.J. Guild, J. Llorca, W. Xu, T. Jafari, P. Toloueinia, D. Kriz, I. Waluyo, R.M. Palomino, J.A. Rodriguez, S.L. Suib, S.D. Senanayake, Cu supported on mesoporous ceria: water gas shift activity at low Cu loadings through metal-support interactions, *Phys. Chem. Chem. Phys.* 19 (2017) 17708–17717, <http://dx.doi.org/10.1039/C7CP02378B>.
- [39] J.-C. Liu, Y.-G. Wang, J. Li, Toward rational design of oxide-supported single-atom catalysts: atomic dispersion of gold on ceria, *J. Am. Chem. Soc.* 139 (2017) 6190–6199, <http://dx.doi.org/10.1021/jacs.7b01602>.
- [40] Y. Wang, J. Ren, K. Deng, L. Gui, Y. Tang, Preparation of tractable platinum, rhodium, and ruthenium nanoclusters with small particle size in organic media, *Chem. Mater.* 12 (2000) 1622–1627, <http://dx.doi.org/10.1021/cm0000853>.
- [41] M. Cargnello, N.L. Wieder, T. Montini, R.J. Gorte, P. Fornasiero, Synthesis of dispersible Pd@CeO₂ core–shell nanostructures by self-assembly, *J. Am. Chem. Soc.* 132 (2010) 1402–1409, <http://dx.doi.org/10.1021/ja909131k>.
- [42] V. Briois, E. Fonda, S. Belin, L. Barthe, C. La Fontaine, F. Langlois, M. Ribbens, F. Villain, SAMBA: the 4–40 keV x-ray absorption spectroscopy beamline at SOLEIL, in: Array (Ed.), UVX 2010 – 10e Colloq. Sur Les Sources Cohérentes Incohérentes UV, VUV X, Appl. Développements Récents, EDP Sciences, Les Ulis, France, 2011, pp. 41–47, , <http://dx.doi.org/10.1051/vuvx/2011006>.
- [43] C. La Fontaine, L. Barthe, A. Rochet, V. Briois, X-ray absorption spectroscopy and heterogeneous catalysis: performances at the SOLEIL's SAMBA beamline, *Catal. Today* 205 (2013) 148–158, <http://dx.doi.org/10.1016/j.cattod.2012.09.032>.
- [44] A.L. Ankudinov, B. Ravel, J.Y. Rehr, S.D. Conradson, Real-space multiple-scattering calculation and interpretation of x-ray-absorption near-edge structure, *Phys. Rev. B* 58 (1998) 7565–7576, <http://dx.doi.org/10.1103/PhysRevB.58.7565>.
- [45] B. Ravel, M. Newville, ATHENA, ARTEMIS, HEPHAESTUS: data analysis for x-ray absorption spectroscopy using IFEFFIT, *J. Synchrotron Radiat.* 12 (2005) 537–541, <http://dx.doi.org/10.1107/S0909049505012719>.
- [46] M. Cargnello, N.L. Wieder, P. Canton, T. Montini, G. Giambastiani, A. Benedetti, R.J. Gorte, P. Fornasiero, A versatile approach to the synthesis of functionalized thiol-protected palladium nanoparticles, *Chem. Mater.* 23 (2011) 3961–3969, <http://dx.doi.org/10.1021/cm2014658>.
- [47] F.A. Bannister, M.H. Hey, Determination of minerals in platinum concentrates from the transvaal by x-ray methods, *Mineral. Mag.* 23 (1932) 188–206, <http://dx.doi.org/10.1180/minmag.1932.023.138.05>.
- [48] J.-H. Zhou, Y.-Z. Li, Z. Liu, X.-T. Chen, Bis[2-mercaptopypyridine N-oxide(1–κ 2N, O] platinum(II), *Acta Crystallogr. Sect. E* 61 (2005) m195–m197, <http://dx.doi.org/10.1107/S1600536804033264>.
- [49] A. Jentys, Estimation of mean size and shape of small metal particles by EXAFS, *Phys. Chem. Chem. Phys.* 1 (1999) 4059–4063, <http://dx.doi.org/10.1039/a904654b>.
- [50] B. Roldan Cuenya, M. Alcántara Ortigoza, L.K. Ono, F. Behafarid, S. Mostafa, J.R. Croy, K. Pareidis, G. Shafai, T.S. Rahman, L. Li, Z. Zhang, J.C. Yang, Thermodynamic properties of Pt nanoparticles: size, shape, support, and adsorbate effects, *Phys. Rev. B: Condens. Matter Mater. Phys.* 84 (2011) 1–14, <http://dx.doi.org/10.1103/PhysRevB.84.245438>.
- [51] C.-M. Lin, T.-L. Hung, Y.-H. Huang, K.-T. Wu, M.-T. Tang, C.-H. Lee, C.T. Chen, Y.-Y. Chen, Size-dependent lattice structure of palladium studied by x-ray absorption spectroscopy, *Phys. Rev. B* 75 (2007) 125426, <http://dx.doi.org/10.1103/PhysRevB.75.125426>.
- [52] S. Mobilio, E. Burattini, A. Balerna, E. Bernieri, P. Picozzi, A. Reale, S. Santucci, K.O. Hodgson, B. Hedman, J.E. Penner-Hahn (Eds.), *Noble Metal Small Cluster EXAFS BT – EXAFS and Near Edge Structure III*, Springer, Berlin Heidelberg, 1984, pp. 222–225.
- [53] D. Bazzin, D. Guillaume, C. Pichon, D. Uzio, S. Lopez, Structure and size of bimetallic palladium–platinum clusters in an hydrotreatment, *Oil Gas Sci. Technol.* 60 (2005) 801–813, <http://dx.doi.org/10.2516/ogst:2005057>.
- [54] F. Bernardi, M.C.M. Alves, A. Traverse, D.O. Silva, C.W. Scheeren, J. Dupont, J. Morais, Monitoring atomic rearrangement in PtxPd_{1-x} (x = 1, 0.7, or 0.5) nanoparticles driven by reduction and sulfidation processes, *J. Phys. Chem. C* 113 (2009) 3909–3916, <http://dx.doi.org/10.1021/jp805465x>.
- [55] M. Monai, T. Montini, C. Chen, E. Fonda, R.J. Gorte, P. Fornasiero, Methane catalytic combustion over hierarchical Pd@CeO₂/Si-Al2O3: effect of the presence of water, *ChemCatChem* 7 (2015) 2038–2046, <http://dx.doi.org/10.1002/cetc.201402717>.
- [56] C. Chen, Y.-H. Yeh, M. Cargnello, C.B. Murray, P. Fornasiero, R.J. Gorte, Methane oxidation on Pd@ZrO₂/Si-Al2O3 is enhanced by surface reduction of ZrO₂, *ACS Catal.* 4 (2014) 3902–3909, <http://dx.doi.org/10.1021/cs501146u>.
- [57] M. Monai, T. Montini, M. Melchionna, T. Duchoň, P. Kúš, C. Chen, N. Tsud, L. Nasi, K.C. Prince, K. Veltruská, V. Matolín, M.M. Khader, R.J. Gorte, P. Fornasiero, The effect of sulfur dioxide on the activity of hierarchical Pd-based catalysts in methane combustion, *Appl. Catal. B: Environ.* 202 (2017) 72–83, <http://dx.doi.org/10.1016/j.apcatb.2016.09.016>.
- [58] S. Zhang, C. Chen, M. Cargnello, P. Fornasiero, R.J. Gorte, G.W. Graham, X. Pan, Dynamic structural evolution of supported palladium–ceria core–shell catalysts revealed by *in situ* electron microscopy, *Nat. Commun.* 6 (2015) 7778, <http://dx.doi.org/10.1038/ncomms8778>.
- [59] M. Borowski, Size determination of small Cu-clusters by EXAFS, *J. Phys. IV* 7 (1997), <http://dx.doi.org/10.1051/jp4/1997190> C2-259–C2-260.
- [60] N. Marinovic, K. Sasaki, R. Adzic, Nanoparticle size evaluation of catalysts by EXAFS: advantages and limitations, *Zast. Mater.* 57 (2016) 101–109, <http://dx.doi.org/10.5937/ZasMat1601101M>.
- [61] T.P. Martin, Shells of atoms, *Phys. Rep.* 273 (1996) 199–241, [http://dx.doi.org/10.1016/0370-1573\(95\)00083-6](http://dx.doi.org/10.1016/0370-1573(95)00083-6).
- [62] C.M.Y. Yeung, K.M.K. Yu, Q.J. Fu, D. Thompsett, M.I. Petch, S.C. Tsang, Engineering Pt in ceria for a maximum metal-support interaction in catalysis, *J. Am. Chem. Soc.* 127 (2005) 18010–18011, <http://dx.doi.org/10.1021/ja056102c>.